

Extreme rainfall triggered the 2018 rift eruption at Kīlauea Volcano

<https://doi.org/10.1038/s41586-020-2172-5>

Jamie I. Farquharson¹ & Falk Amelung¹

Received: 24 July 2019

Accepted: 11 February 2020

Published online: 22 April 2020

 Check for updates

The May 2018 rift intrusion and eruption of Kīlauea Volcano, Hawai'i, represented one of its most extraordinary eruptive sequences in at least 200 years, yet the trigger mechanism remains elusive¹. The event was preceded by several months of anomalously high precipitation. It has been proposed that rainfall can modulate shallow volcanic activity^{2,3}, but it remains unknown whether it can have impacts at the greater depths associated with magma transport. Here we show that immediately before and during the eruption, infiltration of rainfall into Kīlauea Volcano's subsurface increased pore pressure at depths of 1 to 3 kilometres by 0.1 to 1 kilopascals, to its highest pressure in almost 50 years. We propose that weakening and mechanical failure of the edifice was driven by changes in pore pressure within the rift zone, prompting opportunistic dyke intrusion and ultimately facilitating the eruption. A precipitation-induced eruption trigger is consistent with the lack of precursory summit inflation, showing that this intrusion—unlike others—was not caused by the forceful intrusion of new magma into the rift zone. Moreover, statistical analysis of historic eruption occurrence suggests that rainfall patterns contribute substantially to the timing and frequency of Kīlauea's eruptions and intrusions. Thus, volcanic activity can be modulated by extreme rainfall triggering edifice rock failure—a factor that should be considered when assessing volcanic hazards. Notably, the increasingly extreme weather patterns associated with ongoing anthropogenic climate change could increase the potential for rainfall-triggered volcanic phenomena worldwide.

Compelling evidence exists for seismicity generated by rainfall^{4,5}. Rainfall-induced stress changes at depth can promote fault initiation and reactivation—a mechanism invoked for numerous geological phenomena, including landslides⁶, silent slip events⁷ and remote triggering of earthquakes⁸. Rainfall can also interact with hot volcanic lava domes, causing gravitational dome collapse⁹, explosions² and the generation of lahars and other flow phenomena¹⁰. Explosive activity has even been linked to specific weather systems^{2,3}. These mechanisms probably influence volcanic activity only in the upper tens or hundreds of metres¹¹, prompting the suggestion that rainfall may only be a viable trigger for volcanic activity in the shallow subsurface^{12,13}. The only studies to link precipitation to deeper processes consider hydrological loading and unloading of the edifice^{14,15}. The question as to whether and how rainfall can directly induce deep magmatic activity remains unanswered.

In 2018, coincident with prolonged and extreme rainfall, Kīlauea underwent a complex, multistage eruption involving an extensive rift eruption and the collapse of the summit caldera. On 30 April a train of seismicity initiated along the East Rift Zone (ERZ) that was interpreted as a downrift dyke intrusion¹, ultimately breaking ground as a fissure eruption on 3 May, and followed the next day by a magnitude-6.9 earthquake. The summit exhibited numerous explosive eruptions and caldera collapse events that continued through to August; activity at the Lower ERZ was characterized by fissuring and lava fountaining.

This represents one of Kīlauea's most remarkable eruptive sequences over the past two centuries, not least because the initiation mechanism remains equivocal¹. We investigate several lines of evidence that suggest that anomalous rainfall weakened the edifice by instigating an impulsive pressure wave that propagated to depth and modified the local effective stress in the rift zone. We hypothesize that this in turn triggered the dyke intrusion and the eruptive aftermath.

Dyke initiation from a magma chamber can be considered in terms of the static tensile failure criterion around a cavity. Mechanical failure and dyke initiation will be achieved once the magma overpressure, δp_f , achieves a threshold value defined by¹⁶:

$$\delta p_f = \kappa(\varrho g z - [p + \delta p] + \tau) \quad (1)$$

where the product of the rock density, ϱ , gravitational acceleration, g , and depth, z , is the lithostatic stress; p and δp are the hydrostatic pore pressure and the pore-pressure change, respectively; and τ is the tensile strength of the host rock. In an elastic medium, the magma overpressure is proportional to the tangential stress at the chamber wall, and their ratio, κ , is a function of the chamber geometry: for example, $\kappa=2$ for a spherical chamber within an infinite space¹⁷. Equation (1) highlights that—all other things held equal—an increase in pore pressure will decrease the failure overpressure required to initiate chamber-wall

¹Rosenstiel School of Marine and Atmospheric Science, University of Miami, Miami, FL, USA. [✉]e-mail: james.farquharson@rsmas.miami.edu

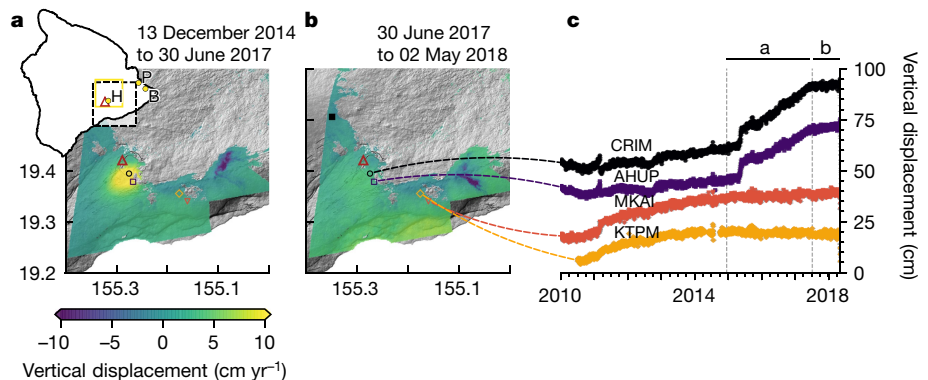


Fig. 1 | Pre-eruption ground deformation of the study site. **a**, Vertical deformation map derived from Sentinel-1InSAR data (ascending track 124 and descending track 87) between December 2014 and June 2017. Inset, map showing the location of Kilauea Volcano (red triangle) and the HVNP rain gauge (H) within the Eastern Rift Zone. The yellow box outlines the $0.25^\circ \times 0.25^\circ$ TRMM/GPM footprint used here. The Paradise Park well (P) and Hawai'i Beaches rain gauge (B) are also highlighted (see Extended Data Fig. 1). The

dashed box indicates the region shown in **a**. **b**, in **b**, the filled square is a reference point; in **a**, **b**, open symbols represent GPS station locations.

b, Vertical deformation between June 2017 and May 2018. **c**, Vertical GPS displacement of the Kilauea flank from 2010. Station names are shown on the panel; colours correspond to locations in **a**, **b**. Dashed vertical lines highlight marked changes-of-slope in station data proximal to the summit (for CRIM and AHUP). Datasets have been offset from the x axis for clarity.

failure and dyke initiation by the amount $\kappa\delta p$. Increasing fluid pressure facilitates not only the initiation of a dyke but also its propagation, in the sense that the fracture toughness (or energy) of the edifice material is dependent on the ambient stress field¹⁸ and thus on the pore pressure. Effective stress (that is, lithostatic stress minus pore pressure) governs the failure stress of volcanic materials¹⁹. During and after heavy rainfall, an impulsive increase in groundwater volume will cause a perturbation in pore pressure at depth, increasing it transiently above the background hydrostatic condition. Under unconfined, saturated conditions typical of basaltic systems, such pore-pressure transients are often reflected by water-level changes in nearby wells²⁰: this is demonstrated in Extended Data Fig. 1, where we correlate rainfall with recorded well data from a site 15 km north of the rift zone. In theory—if the volume and rate of meteoric water infiltration are sufficient—mechanical failure can be induced in the vicinity of a magma chamber or dyke, in turn triggering intrusion or eruption.

Interferometric synthetic-aperture radar (InSAR) data show that more than 0.3 m of uplift occurred at the summit between 2014 and mid-2017 (Fig. 1a), yet only around 0.01 m of uplift was detected at the summit over the following 10 months (Fig. 1b). This temporal deformation pattern is confirmed by data from GPS stations proximal to Kilauea's caldera (CRIM and AHUP), showing that moderate inflation occurred between 2010 and 2015, followed by a substantial increase in inflation rate until around June 2017 (Fig. 1c), after which inflation was negligible for the following 10 months. In the upper and middle ERZ, no substantial inflation was detected between 2010 and 2018 (Fig. 1b; GPS stations MKAI and KTPM in Fig. 1c). This implies that the inflation observed from mid-March¹ reflects local, shallow processes, rather than wholesale pressurization of the system. The lack of precursory summit and rift-zone inflation suggests that the intrusion–eruption was not triggered by an influx of fresh magma from depth but that it was a passive intrusion, caused by extension and/or weakening of the rift zone^{21,22}.

In early 2018, the Hawai'iian islands were subject to protracted, at times extreme, rainfall (Fig. 2). The maximum peak in the rainfall power spectrum occurs at 1 yr^{-1} , indicating substantial annual seasonality in rainfall over Kilauea Volcano on Hawai'i Island (generally, most rainfall occurs between 9 March and 25 August), overlain by a non-negligible stochastic component (Fig. 2b). This annual signal accounts for over half of the variability in rainfall over Kilauea; however, an aseasonal shift of the synoptic-scale atmospheric wave pattern across the North Pacific in mid-to-late January 2018 preceded the passage of several consecutive low-pressure systems over Hawai'i in the months to follow.

Several months of greater than average rainfall culminated in record downpour, with 1.26 m of rain falling within 24 h (14–15 April 2018) on Kauai Island (northwest of Hawai'i Island)—a record not only for Hawai'i but for the entire United States²³. Calibrated precipitation data from NASA's Tropical Rainfall Measurement Mission and Global Precipitation Measurement mission (TRMM/GPM) satellites indicate that over 2.25 m of rainfall fell over Kilauea during the first quarter of 2018, compared with a first-quarter 19-year average of 0.90 m. Figure 2c, e shows the multiday cumulative sum of rainfall calculated as a moving window across the time series, using windows of 30 days (Fig. 2c, approximately 1 month) and 180 days (Fig. 2e, approximately 6 months). These data are lognormal (Fig. 2d, f). Notably, the 30-day total rainfall exceeds 2 standard deviations of the mean ($+2\sigma$) immediately before the 2018 flank eruption: that is, a statistically significant deviation. Even more strikingly, the rolling 180-day cumulative rainfall has only two periods in which rainfall exceeds this threshold, one of which directly precedes the eruption.

Kilauea Volcano is hydrogeologically complex²⁴, as highlighted by laboratory data (for example, see ref.²⁵; see Methods). Accordingly, we model the edifice as two connected saturated domains in a one-dimensional half-space (model α): a highly permeable shallow layer (0–500 m) overlying an intermediate-permeability domain (0.5–10 km). Propagation of pore pressure p from the surface owing to precipitation is modelled using a finite difference approximation to solve for transient, vertical flow of groundwater (that is, the diffusion problem), such that $(\partial p/\partial t) = D(\partial^2 p/\partial z^2)$, where z is depth, t is time and D is hydraulic diffusivity (a function of permeability, bulk modulus, fluid viscosity and porosity). Full details, including parameter values, are given in Methods. For model α , $D = 37\text{ m}^2\text{s}^{-1}$ and $0.34\text{ m}^2\text{s}^{-1}$ above and below 0.5 km (below the surface), respectively (Fig. 3a). Using the calibrated satellite data as a variable-flux boundary, we show the resultant maximum pore-pressure change in Fig. 3b. Three additional models are shown for reference to demonstrate the range of feasible pressure responses to rainfall (see Methods and Extended Data Table 1).

In all modelled scenarios, we observe a quasistatic pore-pressure build-up of tens to thousands of pascals at depths 1–6 km below the surface immediately before the onset of the 2018 flank eruption. For completeness, we include results from the unlikely end-member scenarios in Extended Data Fig. 2. More complex and realistic models yield intermediate pressure changes (Fig. 3b and Extended Data Fig. 2), as demonstrated in Fig. 4a–c. The April 2018 peak in pore pressure is the highest observed throughout the modelled period (for example, see Fig. 4b, c). Parametric analysis of each of the model frameworks shown

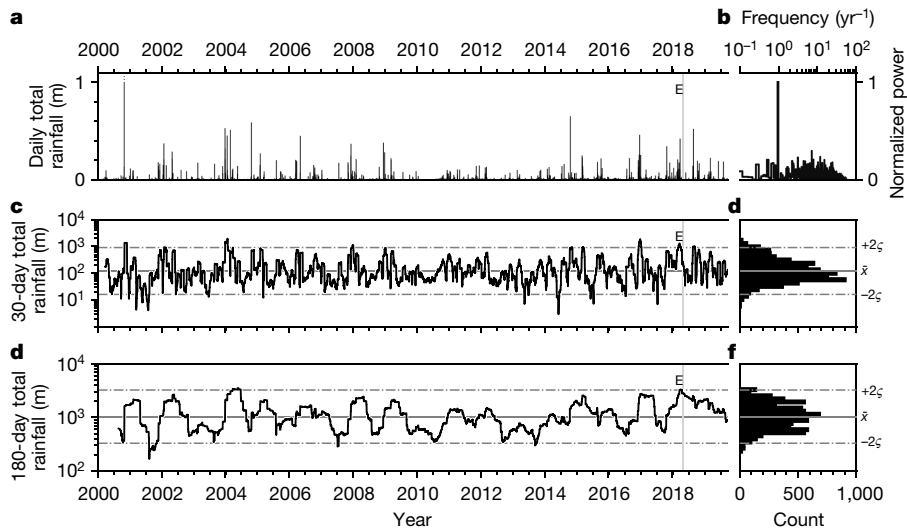


Fig. 2 | Rainfall over Kilauea. **a**, Calibrated daily rainfall amount over Kilauea from March 2000 to July 2019 (TRMM/GPM data calibrated with gauge data; see Fig. 1a inset and Methods). The vertical bar shows the date of flank eruption (E). **b**, Power spectrum of Fourier-transformed rainfall time series (**a**) shown in the (normalized) power–frequency domain. **c**, Rolling 30-day

cumulative rainfall since March 2000 at Kilauea. Horizontal dashed lines delineate two standard deviations either side of the mean ($\bar{x} \pm \sigma$). **d**, Histogram of data in **c** on log-linear axes. **e**, Rolling 180-day cumulative rainfall. **f**, Histogram of data from **e** on log-linear axes.

in Fig. 3a reveals that this pattern holds for a wide range of feasible physical properties. In our preferred model (model α), we obtain pressure changes of around 0.1 kPa and 1 kPa at 3 km and 1 km below the surface, respectively.

At depths of around 3 km below the surface (or 1.8 km below sea level (b.s.l.)), the depth estimated for most lateral magma transport in the rift zone¹), the elevated subsurface pore pressure in early 2018 was the

largest peak in pressure in 47 years—the highest since the onset of the Pu'u 'O'o eruption (Fig. 4b, c). Given the mechanism described above, this is a strong indicator that elevated pore fluid pressures facilitated the 2018 intrusion and rift eruption. Moreover, we outline four independent lines of evidence to support this proposition.

First, there was very little precursory inflation immediately before the rift eruption (Fig. 1b, c). The rapid uplift recorded by tiltmeters in the Pu'u 'O'o area from mid-March reported in ref.¹ thus reflects a highly localized, shallow deformation source. The absence of widespread precursory inflation suggests that the 2018 intrusion was passive, fostered by weakening of the rift zone.

Second, a statistical analysis of the Kilauea's reported historical eruptions shows that the volcano exhibits a marked tendency towards erupting during the wettest times of the year (Extended Data Fig. 3); the onset of around 60% of reported eruptions since 1790 (including the Pu'u 'O'o eruption 1983–2018) occurred during the 'rainy' season, despite the fact that Kilauea's 'rainy' season is shorter than its 'dry' season (see Methods).

Third, recorded intrusions appear to be correlated with elevated pore pressures at depth. Figure 4b shows intrusions into the rift zone since the 1975 Kalapana earthquake (compiled after refs.^{22,26–28}). Comparing the modelled rainfall-induced pressure perturbation at a depth of 3 km below the surface with the long-term average, more than 60% of intrusions (20 of 33) are associated with periods of above-average pore pressure. If we compare the pore-pressure change with the rolling four-year average at the same depth in order to account for interannual fluctuations (such as the El Niño–Southern Oscillation) we find that 19 (58%) were initiated when the pore pressure was above this threshold. Clearly, not every peak in pore pressure is associated with an intrusion, and vice versa—a function of superposing processes with different periodicities (a combination of internal and external forcing), and thus characteristic of triggered systems (see, for example, ref.¹⁴). Nevertheless, it is striking that intrusions are approximately twice as likely to occur at Kilauea when pore pressure is elevated, suggesting that pore pressure can act as a trigger mechanism in a critically stressed—or 'primed'—volcanic system.

Finally, historical precipitation records show that Kilauea's May 1924 eruption—the previous extraordinary eruption—also followed extremely wet conditions. In April 1924, many stations across Hawai'i recorded as much as 0.5 m in excess of the long-term average for that

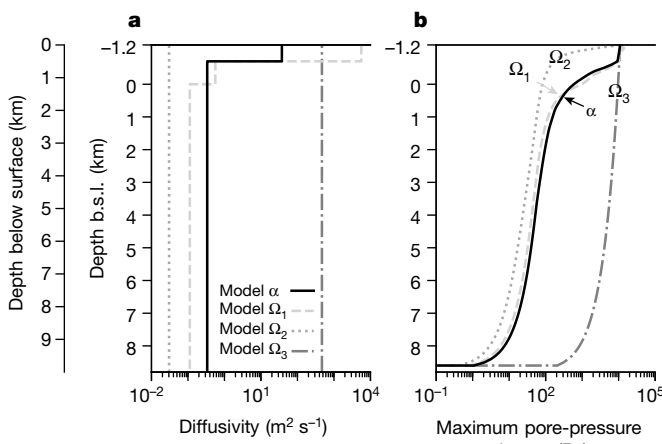


Fig. 3 | Diffusion model metadata. **a**, Diffusivity (a function of permeability, k , bulk modulus, K , fluid viscosity, μ , and porosity, ϕ , given by $kk/\mu\phi$) against depth (depth below the surface and depth b.s.l. are shown for reference) for four different models ($k - \phi$ scenarios, summarized in Extended Data Table 1). The primary model (model α) is a two-layer model, with a zone of high porosity and permeability overlying a lower permeability domain. Reference model Ω_1 subdivides the lower domain into two, each with different properties. Models Ω_2 and Ω_3 are single-domain models, meaning that they use values of porosity, permeability, bulk modulus and viscosity that are constant with depth. See Methods for more details. **b**, The maximum pressure change effected at depth in each model throughout the modelled time series. Note that the maximum pressure change for any given depth can occur on numerous dates and may not be consecutive. For example, high values near the surface may occur frequently (see Fig. 4a, c) but may not propagate to depth. On the other hand, high pressure at depth may not be a direct consequence of a single spike at the surface.

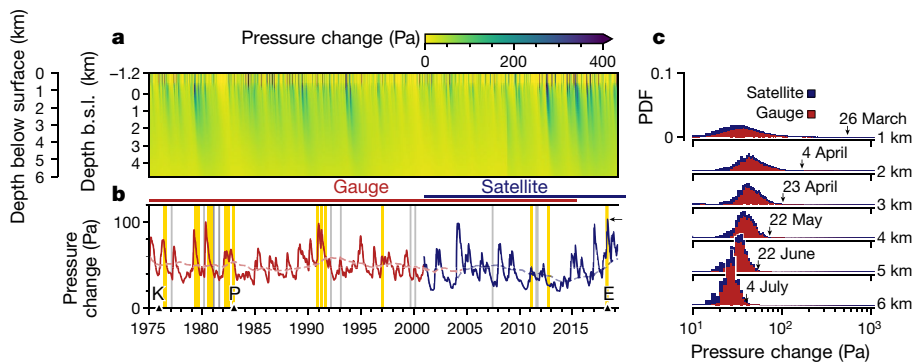


Fig. 4 | Pore-pressure change in response to infiltration into Kilauea's edifice. **a**, Pore-pressure change modelled over the period January 1975 to April 2019, using available HVNP gauge data (1950–2015) and calibrated satellite data (2000–2019), with depth and time. Daily rainfall data are used as a fluctuating boundary condition. Colour scale indicates pressure change. **b**, Pore-pressure change at 3 km below the surface (1.8 km b.s.l.) modelled over the period January 1950 to April 2019 (data shown are since the 1975 Kalapana earthquake). The dashed line shows the four-year running average. K represents the 1975 magnitude-7.2 Kalapana earthquake; P shows the 1983 onset of the Pu'u 'O'o eruption; E represents the 2018 Kilauea rift intrusion–eruption. Vertical bars show reported intrusion events within the rift zone, after refs.^{22,26–28}. Intrusions

are highlighted in yellow if they coincide with periods during which pressure change exceeds the four-year average, and grey if they do not. Intrusion 33 in this time series corresponds to the early 2018 activity (intrusion detected mid-March, followed by the rift eruption on 3 May). The arrow highlights the maximum pore-pressure perturbation over this timeframe (1975 to 2019), coinciding with the onset of 2018's rift eruption. Horizontal bars indicate data availability. **c**, Probability density function (PDF) of modelled pressure change at depths 1–6 km below the surface. Arrows highlight the pore-pressure front diffusing from near the surface (1 km) to greater depths over time (26 March, 4 April, 23 April, 22 May, 22 June and 4 July 2018 at 1 km, 2 km, 3 km, 4 km, 5 km and 6 km below surface).

month, and the gauge measurements for several of these were at that time the highest daily rainfall amounts on record²⁹. In particular, more than 0.1 m fell at the Hawai'i Volcano Observatory in 24 h (14 April). The 2018 eruption echoed many features of 1924 (for example, major summit explosions and a drop in lava lake level), suggesting that not only the timing of intrusions and eruptions but also the eruptive style of Kilauea is influenced by rainfall.

Diffusion modelling shows that rainfall can induce quasistatic pressure changes on the order of kilopascals to tens of kilopascals at depths of a few kilometres (Fig. 4 and Extended Data Fig. 2, respectively). Increasing pore pressure can cause embrittlement³⁰, hydrofracture³¹ and dyke initiation³² by reducing the static threshold for tensile failure. Although the precise magnitude of stress change will vary owing to drainage and the thermal contribution of the magma, pressure changes on the order of 1 kPa are in line with trigger stresses caused by solid Earth tides^{33–35} and those required to trigger earthquakes on pre-existing faults³⁶. Pressure changes on the order of 10 kPa are typically assumed to be necessary to trigger mechanical failure and attendant geological processes in unstressed media⁴; however, it has been demonstrated that stress changes in the range of 0.1–1 kPa are sufficient for rainfall to trigger earthquakes provided that the crust is in a critical state⁵. It has been inferred from historical eruption patterns that Kilauea is particularly sensitive to external modulation and eruption triggering²⁶; moreover, recent evidence shows that the rift zone has undergone mechanical weakening over the course of the Pu'u 'O'o eruption³⁷. Although we do not account here for potential amplification or dampening of the precipitation-induced pressure change in response to poroelastic effects, our results show that the quasistatic stress changes associated with pore-pressure infiltration can effect a sustained increase above long-term background levels in a way that dynamic stresses of similar magnitude (for example, solid Earth tides) cannot. Relatively small changes in edifice pore pressure can result in a substantial reduction in the overpressure required to instigate magma chamber failure (Equation (1)). As such, precipitation-induced pore-pressure fluctuations contribute to the overall stress state of Kilauea Volcano; we propose that this hydromechanical coupling may directly trigger primary volcanic activity.

The unprecedented rainfall over Hawai'i in the months before the 2018 flank eruption increased the potential for mechanical failure within the edifice. Taken together, the separate lines of evidence

reported above strongly suggest a correlation between rainfall and volcanic activity at Kilauea—not only in 2018, but throughout its eruptive history. By locally reducing effective stress at depth, prolonged periods of rainfall may induce opportunistic dyke intrusions or facilitate dyke propagation. The historical preponderance of Kilauea's eruptions during the wettest parts of the year buttresses this theory, as does the coincidence of dyke intrusions with elevated subsurface pore pressure and the similarities observed between volcanic events associated with similar rainfall patterns. Critically, as our climate continues to change, the occurrence of prolonged periods of extreme rainfall is predicted to increase in many parts of the world, increasing the potential for rainfall-triggered volcanic phenomena. Elevated pore pressures at depth tend to be fostered and maintained by prolonged periods of above-average rainfall, associated with long-lived and generally forecastable synoptic-scale systems: by better understanding the hydromechanical couplings between rainfall and volcanism, advanced warning of rainfall-induced volcanic hazards may be achievable.

Online content

Any methods, additional references, Nature Research reporting summaries, source data, extended data, supplementary information, acknowledgements, peer review information; details of author contributions and competing interests; and statements of data and code availability are available at <https://doi.org/10.1038/s41586-020-2172-5>.

- Neal, C. A. et al. The 2018 rift eruption and summit collapse of Kilauea Volcano. *Science* **363**, 367–374 (2019).
- Mastin, L. G. Explosive tephra emissions at Mount St. Helens, 1989–1991: the violent escape of magmatic gas following storms? *Geol. Soc. Am. Bull.* **106**, 175–185 (1994).
- Matthews, A. J. & Barclay, J. A thermodynamical model for rainfall-triggered volcanic dome collapse. *Geophys. Res. Lett.* **31**, L05614 (2004).
- Costain, J. K. Groundwater recharge as the trigger of naturally occurring intraplate earthquakes. *Geol. Soc. Lond. Spec. Publ.* **432**, 91–118 (2017).
- Hainzl, S., Kraft, T., Wassermann, J., Igel, H. & Schmedes, E. Evidence for rainfall-triggered earthquake activity. *Geophys. Res. Lett.* **33**, L19303 (2006).
- Handwerger, A. L., Rempel, A. W., Skarbek, R. M., Roering, J. J. & Hillley, G. E. Rate-weakening friction characterizes both slow sliding and catastrophic failure of landslides. *Proc. Natl Acad. Sci. USA* **113**, 10281–10286 (2016).
- Kodaira, S. et al. High pore fluid pressure may cause silent slip in the Nankai Trough. *Science* **304**, 1295–1298 (2004).
- Prejean, S. G. et al. Remotely triggered seismicity on the United States west coast following the M_w 7.9 Denali Fault earthquake. *Bull. Seismol. Soc. Am.* **94**, S348–S359 (2004).

9. Voight, B., Constantine, E. K., Sisowidjoyo, S. & Torley, R. Historical eruptions of Merapi volcano, central Java, Indonesia, 1768–1998. *J. Volcanol. Geotherm. Res.* **100**, 69–138 (2000).
10. Yamasato, H., Kitagawa, S. & Komiya, M. Effect of rainfall on dacitic lava dome collapse at Unzen volcano, Japan. *Pap. Meteorol. Geophys.* **48**, 73–78 (1998).
11. Christenson, B. W. et al. Cyclic processes and factors leading to phreatic eruption events: insights from the 25 September 2007 eruption through Ruapehu Crater Lake, New Zealand. *J. Volcanol. Geotherm. Res.* **191**, 15–32 (2010).
12. Canon-Tapia, E. Volcanic eruption triggers: a hierarchical classification. *Earth Sci. Rev.* **129**, 100–119 (2014).
13. Matthews, A. J., Barclay, J. & Johnstone, J. E. The fast response of volcano-seismic activity to intense precipitation: triggering of primary volcanic activity by rainfall at Soufrière Hills Volcano, Montserrat. *J. Volcanol. Geotherm. Res.* **184**, 405–415 (2009).
14. Violette, S. et al. Can rainfall trigger volcanic eruptions? A mechanical stress model of an active volcano: ‘Piton de la Fournaise’, Reunion Island. *Terra Nova* **13**, 18–24 (2001).
15. Hammond, W. C., Kreemer, C., Zaliapin, I. & Blewitt, G. Drought-triggered magmatic inflation, crustal strain and seismicity near the Long Valley Caldera, Central Walker Lane. *J. Geophys. Res. Solid Earth* **124**, 6072–6091 (2019).
16. Timoshenko, S. P. & Goodier, J. *Theory of Elasticity* 2nd edn (Maple Press, 1951).
17. Tait, S., Jaupart, C. & Vergniolle, S. Pressure, gas content and eruption periodicity of a shallow, crystallising magma chamber. *Earth Planet. Sci. Lett.* **92**, 107–123 (1989).
18. Rubin, A. M. Tensile fracture of rock at high confining pressure: implications for dike propagation. *J. Geophys. Res. Solid Earth* **98** (B9), 15919–15935 (1993).
19. Wong, T. F. & Baud, P. The brittle-ductile transition in porous rock: a review. *J. Struct. Geol.* **44**, 25–53 (2012).
20. Jónsson, S., Segall, P., Pedersen, R. & Björnsson, G. Post-earthquake ground movements correlated to pore-pressure transients. *Nature* **424**, 179–183 (2003).
21. Owen, S. et al. January 30, 1997 eruptive event on Kilauea Volcano, Hawaii, as monitored by continuous GPS. *Geophys. Res. Lett.* **27**, 2757–2760 (2000).
22. Poland, M. P., Takahashi, T. J. & Landowski, C. M. *Characteristics of Hawaiian Volcanoes* Professional Paper 1801 (Government Printing Office, 2014).
23. National Climate Extremes Committee. *National Record 24-Hour Precipitation at Waipā Garden, Hawai'i Report 14 December 2018* (National Centers for Environmental Information, 2018).
24. Ingebritsen, S. E. & Scholl, M. A. The hydrogeology of Kilauea volcano. *Geothermics* **22**, 255–270 (1993).
25. Keller, G. V., Grose, L. T., Murray, J. C. & Skokan, C. K. Results of an experimental drill hole at the summit of Kilauea Volcano, Hawaii. *J. Volcanol. Geotherm. Res.* **5**, 345–385 (1979).
26. Klein, F. W., Koyanagi, R. Y., Nakata, J. S. & Tanigawa, W. R. in *U.S. Geological Survey Professional Paper, Issue 1350 Vol. 2* (eds Decker, R. W. et al.) 1019–1185 (US Geological Survey, 1987).
27. Heliker, C. & Mattox, T. N. *The First Two Decades of the Pu'u 'O'o-Kūpaianaha Eruption: Chronology and Selected Bibliography* (U.S. Geological Survey, 2003).
28. Orr, T. R. et al. in *Hawaiian Volcanoes: From Source to Surface Vol. 208*, Ch. 19 (eds Carey, R. et al.) 393–420 (2015).
29. Loveridge, E. F. April 1924 climatological data: Hawaii section. *Climatological Data* **4**, 25–40 (1924).
30. Farquharson, J., Heap, M. J., Baud, P., Reuschlé, T. & Varley, N. R. Pore pressure embrittlement in a volcanic edifice. *Bull. Volcanol.* **78**, 6 (2016).
31. Gudmundsson, A. *Rock Fractures in Geological Processes* (Cambridge Univ. Press, 2011).
32. Albino, F., Amelung, F. & Gregg, P. The role of pore fluid pressure on the failure of magma reservoirs: insights from Indonesian and Aleutian arc volcanoes. *J. Geophys. Res. Solid Earth* **123**, 1328–1349 (2018).
33. Tolstoy, M., Vernon, F. L., Orcutt, J. A. & Wyatt, F. K. Breathing of the seafloor: tidal correlations of seismicity at Axial volcano. *Geology* **30**, 503–506 (2002).
34. Scholz, C. H., Tan, Y. J. & Albino, F. The mechanism of tidal triggering of earthquakes at mid-ocean ridges. *Nat. Commun.* **10**, 2526 (2019).
35. Dzurisin, D. Influence of fortnightly earth tides at Kilauea volcano, Hawaii. *Geophys. Res. Lett.* **7**, 925–928 (1980).
36. Saar, M. O. & Manga, M. Seismicity induced by seasonal groundwater recharge at Mt. Hood, Oregon. *Earth Planet. Sci. Lett.* **214**, 605–618 (2003).
37. Wauthier, C., Roman, D. C. & Poland, M. P. Modulation of seismic activity in Kilauea's upper East Rift Zone (Hawai'i) by summit pressurization. *Geology* **47**, 820–824 (2019).

Publisher's note Springer Nature remains neutral with regard to jurisdictional claims in published maps and institutional affiliations.

© The Author(s), under exclusive licence to Springer Nature Limited 2020

Methods

Rainfall data

To obtain a contiguous rainfall time series at Kilauea, we extract precipitation data for the period March 2000 to June 2019 from the NASA/JAXA Tropical Rainfall Measuring Mission (TRMM) and Global Precipitation Measurement (GPM) satellite datasets, which are operationally available from NASA from March 2000. We use the 3B42 Research Version product (<https://doi.org/10.5067/TRMM/TMPA/3H/7>), a $0.25 \times 0.25^\circ$ gridded daily product resampled from the original three-hourly rainfall estimates. Although this provides a daily rainfall estimate over the entire time frame, these data are an areal average and under-represent the true volume of rainfall at Kilauea by a factor, Λ , of 5.12. We calibrate the satellite data using rain gauge data available between 1950 and 2015 (gauge H in Fig. 1a, inset). The gauge data are from the Hawai'i Volcano National Park rainfall gauge (Global Historical Climatological Network Daily (GHCND) identification code USC00511303), available through the Climate Data Online project of the National Oceanic and Atmospheric Administration (NOAA). This gauge site was a volunteer observer station which closed as of 22 June 2015.

Ground deformation

Vertical velocity data were obtained by processing Sentinel-1 ascending and descending SAR data. Data were processed using the US Jet Propulsion Laboratory (JPL)-developed InSAR Scientific Computing Environment (ISCE) open-source software package³⁸, and further time-series analysis was performed using the MintPy software toolbox (Miami INsar Time-series software in PYthon), developed at the University of Miami³⁹. Vertical GPS data (Fig. 1c) were accessed from the Nevada Geodetic Laboratory for GPS stations CRIM, AHUP, KTPM and MKAI (Fig. 1a, b; <http://geodesy.unr.edu/NGLStationPages/stations/>; ref. ⁴⁰). Vertical data are extracted directly with associated vertical error.

Modelling approach

We model the subsurface pore-pressure perturbation as a function of rainfall by using a finite difference approximation to solve for a transient, vertical flow of groundwater (that is, the diffusion problem), such that $(\partial p/\partial t) = [kK/\mu\phi][\partial^2 p/\partial z^2]$. Here, pore pressure, p , over time, t , and depth, z , beneath the surface is a function of the permeability, k , the bulk modulus, K , and the porosity, ϕ , of the edifice, as well as the viscosity, μ , of the percolating fluid (water). The expression $kK/\mu\phi$ represents the (hydraulic) diffusion coefficient. Assuming a zero-flux boundary, we impose a pressure change of zero at the base, Z , of the domain, which is arbitrarily given as 10 km below the surface (8.8 km b.s.l.), that is, $(\partial p/\partial z)|_{z=Z} \approx \delta p|_{z=Z} = 0$. We note that this is deep enough that we do not observe boundary effects in the depth range of interest. Although subsurface pressure data for calibration are scarce, this solution appears to reflect pressure changes at depth well (Extended Data Fig. 1), as it relies on physical parameters.

Pressure at the surface is defined given the calibrated height of recorded rainfall, h , the density of water, ρ_w , and the acceleration due to gravity, g , such that $p(z=0, t) = \rho_w g h(t)$, where $\Lambda = 5.12$ is the calibration factor described above, and z represents the depth below the ground surface. To test the sensitivity of our model to the rainfall input, we also ran it assuming daily rainfall values of $\pm 10\%$ of the recorded value: we note that the relative timing and magnitude of pressure evolution varies negligibly as a result.

The uppermost 500 m or so of the Kilauea volcano comprises some of the planet's most permeable known geological materials (with permeabilities on the order of 10^{-10} m 2 , on the basis of laboratory measurements²⁵ and simulations⁴¹). Vertical permeability, k_z , however, is as much as three orders of magnitude lower than horizontal permeability, k_x (refs. ^{24,42})—a consequence of surface-parallel layering anisotropy⁴³. Below the water table, equivalent (bulk) permeability is anticipated to be lower still. Modelling and mud-loss permeabilities⁴⁴ suggest

that k_x is in the range 1×10^{-14} m 2 to 6×10^{-14} m 2 , with k_z estimated to be perhaps a factor of 10 or 100 lower, but not less than around 10^{-16} m 2 (ref. ⁴⁵). This is greater than laboratory measurements in this interval, partially because large-scale fractures are not encompassed by such measurements⁴³, and partially because sample recovery of friable, high-permeability materials is inherently low²⁵. Reference²⁵ reports modal porosity values of edifice-forming basalt at Kilauea of 0.15–0.3. This range is in agreement with a wealth of experimental data⁴⁶ for the typical porosity of a volcanic edifice. Thanks to these studies, we have a reasonable site-specific estimate of the permeable architecture beneath Kilauea.

Deformation experiments on edifice-forming volcanic materials⁴⁷ reveal typical values of pore compressibility (β , the inverse of the bulk modulus) on the order 10^{-10} Pa $^{-1}$. Accordingly, we assume a value of $K = \beta^{-1} = 10$ GPa throughout this study. Interstitial fluid (water) viscosity, μ , is similarly assumed to be constant (8.9×10^{-4} Pa s $^{-1}$). Permeability and porosity (the remaining parameters governing rainwater percolation through the edifice) are neither constant with depth nor independent of each other, however. Our preferred model (model α) comprises two domains in a one-dimensional half-space, the uppermost of which is highly permeable and porous ($k = 1 \times 10^{-12}$ m 2 and $\phi = 0.3$). The underlying portion, deeper than 500 m, is less permeable (6×10^{-15} m 2) and less porous ($\phi = 0.2$). For convenience, these data are shown in Extended Data Table 1. The results of three different additional models are shown in Fig. 3. The first is a three-section model (here called model Ω_1), which assumes that the upper 500 m of the edifice overlies intermediate- and low-permeability domains. Model Ω_2 and model Ω_3 are both homogeneous equivalent permeability models (that is, a single value of permeability is used throughout the domain), based on the parameters of model Ω_1 . Model Ω_2 reflects the arithmetic average permeability of the domains in model Ω_1 ($k_x = 8.3 \times 10^{-13}$ m 2), while model Ω_3 uses the geometric average permeability of the domains in model Ω_1 : $k_x = 5.4 \times 10^{-16}$ m 2 . Values are given in Extended Data Table 1. Note that these latter models represent extreme and unlikely end-members and are shown here only for completeness.

The homogenous models (Ω_2 and Ω_3) essentially represent upper and lower bounds of the pressure change at depth, even though the heterogeneous models may contain domains of lower equivalent permeability. Model Ω_2 exhibits very little pressure attenuation of pressure with depth and time because of the high permeability value assumed, and may be representative of an extensively fractured edifice in a self-organized critical state⁴⁸, which gives rise to hydraulic continuity from the surface to depths of several kilometres (that is, close to the pressure response of a theoretical kilometres-long vertical crack). Despite the rapid attenuation of model Ω_3 (based on the geometric average permeability), we highlight that a pressure perturbation of over 0.1 kPa is still observed at 3 km depth. The geometric average is thought to be a reasonable compromise between direction-specific averaging approaches where the precise geometry and orientation of an anisotropic medium is unknown⁴³, and so represents an approximation of a series of randomly oriented unfractured geological units. Relative to these homogenous scenarios, the heterogeneous models (α and Ω_1) yield intermediate deviations in pressure, and comparing these models with the limited well-level data available indicate that they capture the evolution of subsurface fluid pressure in our study area (Extended Data Fig. 1). In all modelled scenarios we observe a build-up of pore pressure of tens to thousands of pascals at a depth of 3 km immediately before the onset of the 2018 rift eruption. Exploring the (k, ϕ, z) parameter space for each of the model frameworks shown in Fig. 3a reveals that this pattern holds for a wide range of feasible physical properties in a depth interval generally assumed to accommodate magma transport between Kilauea's relatively shallow magma source and the surface. In particular, this April 2018 peak is observed when the diffusivity coefficient falls within the range 0.1–1.0 for the majority of the edifice, a range in agreement with other studies that investigate fluid percolation

through volcanic media^{36,49,50} and corresponding to a wide range of physically tractable combinations of k and ϕ .

Observed well-level data

There is a paucity of available subsurface pore-pressure data for Kilauea. Reference⁵⁰ shows pore-pressure data collected for a few weeks in 2001; in this case, the time series is too short and the signal from a coincident magmatic intrusion too strong to detect the input of meteoric water. In earlier work⁵¹, pressure or head data are reported for a number of wells throughout the region around Kilauea, but are generally heavily modulated by ocean tides or located far from the rift zone. Despite these known issues, we show a time series of well-level change data digitized from ref.⁵¹, in order to highlight that a diffusion-based modelling approach is appropriate for describing groundwater evolution within the East Rift Zone (see also refs.^{50,52}). The head data are derived from aquifer tests performed in the early 1990s at the Paradise Park well (located at longitude -154.976 , latitude 19.596 ; state well number 3588-01; see Fig. 1a inset), located approximately 15 km north of the rift zone, for which there is a near-continuous record between October 1992 and September 1993. Reference⁵¹ highlights that the well is located in a portion of the aquifer that effectively dampens the tidal signal, meaning that the primary influence recorded ought to be that of the rainfall. We model pore-pressure evolution using rainfall as an input, as described in the ‘Modelling approach’ section above. In this case, we use data from the Hawai‘ian Beaches rain gauge (approximately 9 km southeast from the Paradise Park well; see Fig. 1a inset), available between September 1992 and August 2005. For simplicity’s sake, we use the same input parameters as determined for Kilauea Volcano itself (based on collated experimental, modelling and drilling data), although we acknowledge that the subsurface structure at Paradise Park may differ somewhat. Because our diffusion model solely comprises physical, measurable parameters (permeability, porosity and so on), there should be no need—in theory—to tune it empirically, provided that our knowledge of the subsurface physical properties is sufficient.

Extended Data Fig. 1b shows the well-level change data⁵¹, alongside the pore-pressure change data at 1 km depth modelled here on the basis of rainfall records from the Hawai‘i Beaches gauge (Extended Data Fig. 1a; see Fig. 1a inset for location). Although some discrepancies remain, clearly the modelling approach used here reproduces much of the subsurface pressure response resulting from rainfall infiltration (in particular the timing and relative magnitude of peaks, as highlighted by the grey bars). As such, we consider this model appropriate to describe subsurface pore-pressure evolution within the rift zone without empirically varying the diffusivity parameter, D .

Additional model results

Four models are described in the main text, with results shown from our preferred model, α . For reference, results from the three additional models are shown in Extended Data Fig. 2.

The parameters of model Ω_1 are based on previous experimental, numerical and in situ drilling data (see the ‘Modelling approach’ section above). Note that the maximum pore pressure occurs immediately before the 2018 fissure eruption (Extended Data Fig. 2). Based on model Ω_1 , 64% of intrusions (21 out of 33) occur when pore pressure is above the four-year average. Models Ω_2 and Ω_3 represent theoretical end-member values for hydraulic diffusivity within the East Rift Zone, and do not necessarily reflect realistic pressure-evolution scenarios. Twelve per cent of intrusions (4 of 33) occur when pore pressure is above the four-year average for Ω_2 . Fifty-five per cent of intrusions (18 of 33) occur when pore pressure is above the four-year average for Ω_3 .

Binomial probability analysis of eruption record

Fourier analysis of the satellite-derived rainfall time series (see, for example, Fig. 2) reveals that rain falls over Kilauea predominantly between 9 March and 25 August, which we define as the ‘wet’ season.

This period covers 46% of the year and accumulates >64% of annual rainfall. We analyse Kilauea’s eruption record (based on the onset date of eruptions defined in the Smithsonian Institution’s Global Volcanism Program eruption database: <https://volcano.si.edu/volcano.cfm?vn=332010>). Note that this includes the onset of the 1983 Pu‘u ‘Ō‘ō eruption. If eruptions were randomly (or uniformly) distributed throughout the year, we would anticipate them to occur during the ‘wet’ season with a probability of around 0.46. However, the ratio of ‘wet’-season to ‘dry’-season historical eruptions is more than 0.58. We can assess the prevalence of eruptions occurring during the ‘wet’ season by using binomial probability analysis based on the modelled time-series and Kilauea’s eruption record. The probability is calculated by:

$$\wp(x) = [n!/x!(n-x)!]\wp^x(1-\wp)^{n-x}$$

where $\wp(x)$ is the probability of ‘successes’ out of n trials; \wp is the probability of success of a given trial (we define a ‘success’ as an eruption that occurs within the predefined ‘rainy’ season for Kilauea); and n corresponds to the total number of observed eruptions in our dataset. This analysis allows us to determine the probability of the observed ratio of ‘wet’-season eruptions to ‘dry’-season eruptions occurring fortuitously. The mean and standard deviation of this distribution are given by $\bar{x} = n\wp$ and $\zeta = \sqrt{\bar{x}(1-\wp)}$, respectively.

The observed value (Extended Data Fig. 3) is just within the conventional 2ζ range, which suggests that it could be a fortuitous distribution (that is, many more eruptions could have occurred during the ‘wet’ season by chance). Although this result in isolation precludes strong statistical inferences from being drawn, we highlight that the observed trend for eruptions to occur predominantly in the ‘wet’ season mirrors the prevalence of dyke intrusions occurring during periods of elevated subsurface pore pressure (approximately 60% of historical eruptions and recent dykes are associated with rainfall). We repeat the same analysis using only eruptions defined by the Global Volcanism Program as having an explosivity index value (VEI) of two or greater. Although there are too few reported larger eruptions to be statistically robust, we highlight that, again, the number of eruptions is significantly higher (to the one-sigma level) during the ‘wet’ season (four out of five VEI 2+ eruptions occurred during the ‘wet’ season; see Extended Data Fig. 3).

Data availability

Satellite-derived rainfall data (TRMM and GPM satellite data) are available from NASA’s EarthData GES DISC portal (<https://doi.org/10.5067/TRMM/TMPA/3H/7>). Rainfall gauge data are available from the NOAA’s National Centers for Environmental Information climate data portal (<https://www.ncdc.noaa.gov/cdo-web/datasets/GHCND/stations/GHCND:USC00511303/detail>). Vertical GPS data are available from the Nevada Geodetic Laboratory (<http://geodesy.unr.edu/NGLStation-Pages/stations/>; stations CRIM, AHUP, MKAI and KTPM). Additional datasets generated here are available from the corresponding author on reasonable request. Sentinel-1 ascending- and descending-track SAR acquisitions were obtained through Unavco’s Seamless SAR Archive (<https://github.com/bakerunavco/SSARA>). Vertical displacement (velocity) maps of Kilauea for the time periods 2014–2017 and 2018 are available at <https://doi.org/10.5281/zenodo.3459589>, alongside the Shuttle Radar Tomography Mission (SRTM) digital elevation model used for plotting data.

Code availability

An archived version of the code required for data access, analysis and display is available at <https://doi.org/10.5281/zenodo.3635944>. Python code is in a Jupyter Notebook. Version updates, if applicable, will be made available via GitHub: https://github.com/jifarquharson/Farquharson_Amelung_2020_Kilauea-Nature and <https://github.com/>

Article

geodesymiami/papers/tree/master/Farquharson_Amelung_2020_Kilauea-Nature.

38. Fattah, H., Agram, P. & Simons, M. A network-based enhanced spectral diversity approach for TOPS time-series analysis. *IEEE Trans. Geosci. Remote Sens.* **55**, 777–786 (2017).
39. Yunjun, Z., Fattah, H. & Amelung, F. Small baseline InSAR time series analysis: unwrapping error correction and noise reduction. *Computers Geosci.* **133**, 104331 (2019).
40. Blewitt, G., Hammond, W. C. & Kreemer, C. Harnessing the GPS data explosion for interdisciplinary science. *Eos* **99**, <https://doi.org/10.1029/2018EO104623> (2018).
41. Imada, J. A. *Numerical Modeling of the Groundwater in the East Rift Zone of Kilauea Volcano, Hawaii*. PhD Thesis, Univ. Hawaii at Manoa (1984).
42. Souza, W. R. & Voss, C. I. Analysis of an anisotropic coastal aquifer system using variable-density flow and solute transport simulation. *J. Hydrol.* **92**, 17–41 (1987).
43. Farquharson, J. I. & Wadsworth, F. B. Upscaling permeability in anisotropic volcanic systems. *J. Volcanol. Geotherm. Res.* **364**, 35–47 (2018).
44. Murray, J. C. *The Geothermal System at Kilauea Volcano, Hawaii*. PhD Thesis, Colorado School of Mines, Golden (1974).
45. Hsieh, P. A. & Ingebritsen, S. E. Groundwater inflow toward a preheated volcanic conduit: application to the 2018 eruption at Kilauea Volcano, Hawai'i. *J. Geophys. Res. Solid Earth* **124**, 1498–1506 (2019).
46. Farquharson, J., Heap, M. J., Varley, N. R., Baud, P. & Reuschlé, T. Permeability and porosity relationships of edifice-forming andesites: a combined field and laboratory study. *J. Volcanol. Geotherm. Res.* **297**, 52–68 (2015).
47. Heap, M. J. & Wadsworth, F. B. Closing an open system: pore pressure changes in permeable edifice rock at high strain rates. *J. Volcanol. Geotherm. Res.* **315**, 40–50 (2016).
48. Bak, P., Tang, C. & Wiesenfeld, K. Self-organized criticality: an explanation of the 1/f noise. *Phys. Rev. Lett.* **59**, 381 (1987).
49. Gao, S. S., Silver, P. G., Linde, A. T. & Sacks, I. S. Annual modulation of triggered seismicity following the 1992 Landers earthquake in California. *Nature* **406**, 500–504 (2000).
50. Hurwitz, S. & Johnston, M. J. Groundwater level changes in a deep well in response to a magma intrusion event on Kilauea Volcano, Hawai'i. *Geophys. Res. Lett.* **30**, 2173 (2003).
51. Gingerich, S. B. *The Hydrothermal System of the Lower East Rift Zone of Kilauea Volcano: Conceptual and Numerical Models of Energy and Solute Transport*. PhD thesis, Univ. Hawaii (1995).
52. Cervelli, P., Segall, P., Johnson, K., Lisowski, M. & Miklius, A. Sudden aseismic fault slip on the south flank of Kilauea volcano. *Nature* **415**, 1014–1018 (2002); corrigendum **418**, 108 (2002).

Acknowledgements This study would not have been possible without the Tropical Rainfall Measuring Mission (TRMM) and the Global Precipitation Measurement Mission (GPM)—joint missions between the National Aeronautics and Space Administration (NASA) and the Japanese Space Exploration Agency (JAXA)—and the European Space Agency's (ESA) Copernicus Sentinel-1 data. Copernicus Sentinel-1 data with six-day imagery are available thanks to the Group on Earth Observation's (GEO) Geohazard Supersites and Natural Laboratory Initiative (GSNL). This work was supported by funding from the NASA's Interdisciplinary Research in Earth Science (IDS) program (grant number 80NSSC17K0028 P00003). Data processing was conducted at the High Performance Computing core of the University of Miami's Center for Computational Science (CCS) using the public domain ISCE and SSARA softwares of the Jet Propulsion Laboratory (JPL) and Unavco, respectively. This study was motivated by preliminary analysis by F. Albino, and has benefited from discussions with I. Johanson, K. Anderson and D. Swanson, as well as the comments of three reviewers. Y. Zhang is thanked for his work in the development of MintPy (<https://github.com/insarlab/MintPy>). We thank NASA, the Nevada Geodetic Laboratory and the NOAA for making the data used herein freely available, as well as the developers of SSARA, ISCE and MintPy for providing free open-source software. We acknowledge Hawai'i as an indigenous space whose original people are today identified as Native Hawaiians.

Author contributions J.I.F. and F.A. conceived the study. J.I.F. performed the modelling and wrote the initial draft of the manuscript. F.A. processed the InSAR data. Both authors contributed to the discussion and interpretation of the results, and the writing of the paper.

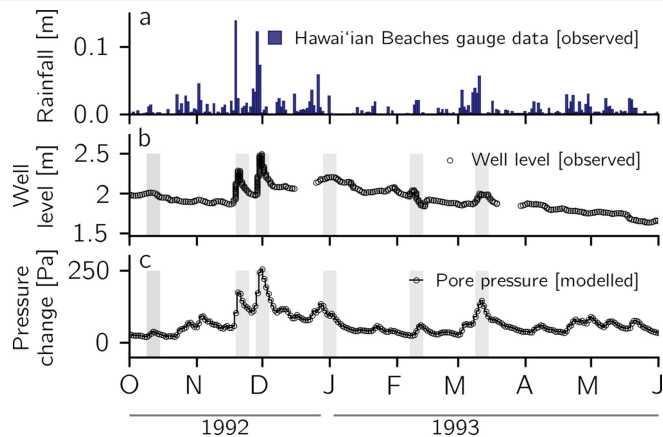
Competing interests The authors declare no competing interests.

Additional information

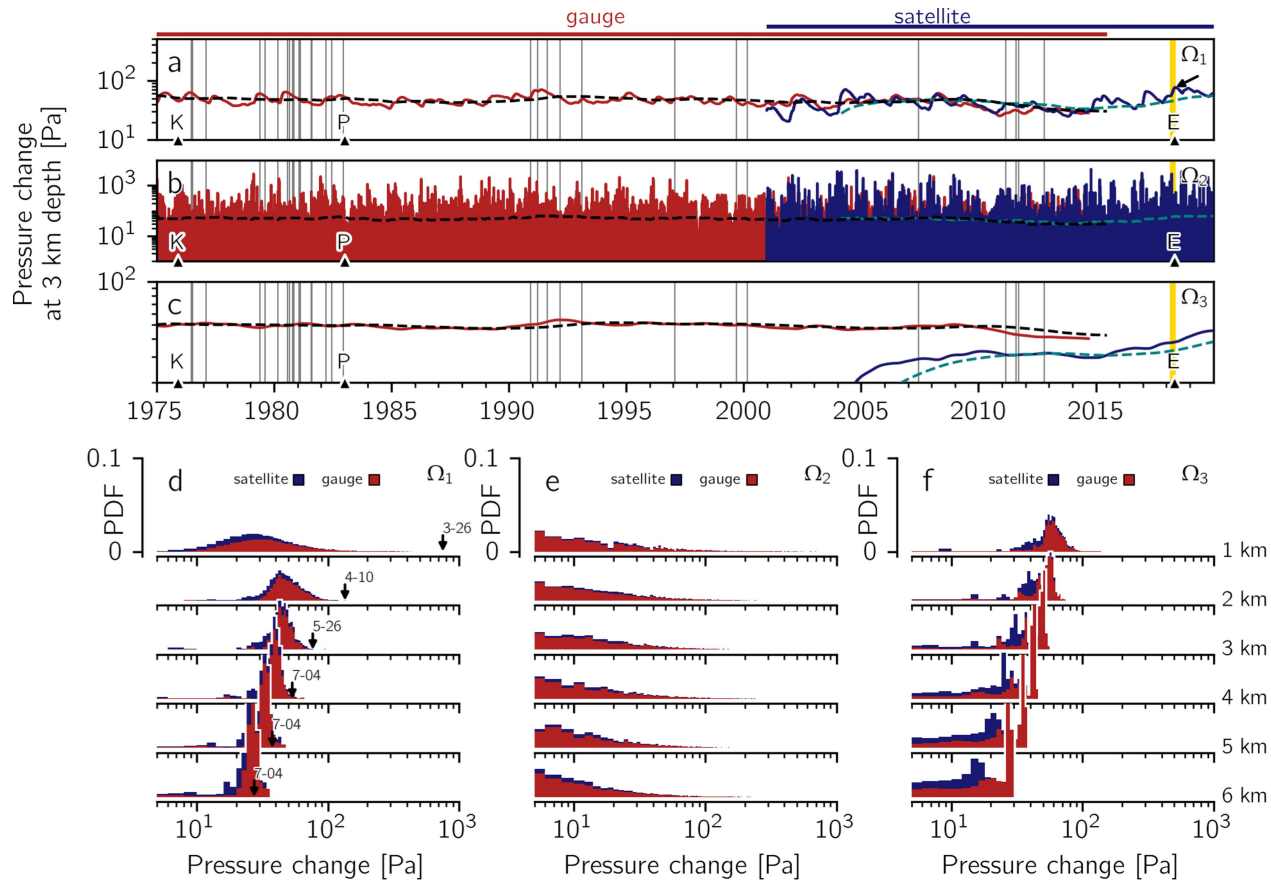
Correspondence and requests for materials should be addressed to J.I.F.

Peer review information *Nature* thanks Michael Manga and the other, anonymous, reviewer(s) for their contribution to the peer review of this work.

Reprints and permissions information is available at <http://www.nature.com/reprints>.

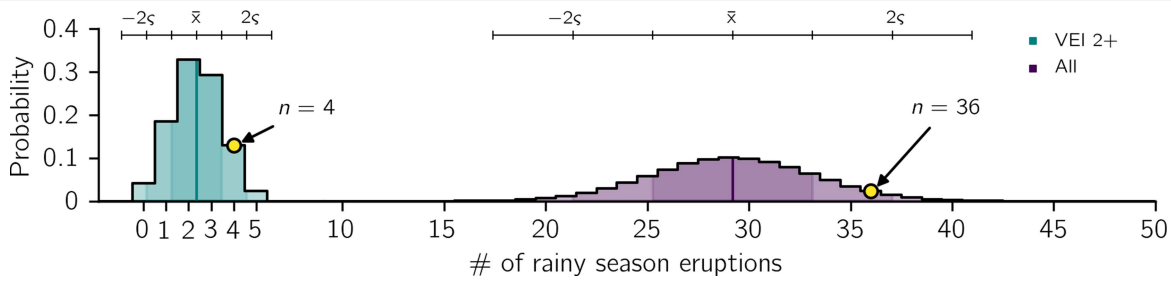


Extended Data Fig. 1 | Comparison of recorded head change and modelled pressure change. **a**, Rainfall data obtained from the Hawai‘ian Beaches rain gauge (refer to Fig. 1a inset for location). **b**, Data from the Paradise Park well (see Fig. 1a inset for the location of the well), digitized from ref.⁵¹ over the time period October 1992–June 1993. **c**, Pressure evolution at a depth of 1 km modelled using rain data from **a**. Grey bars highlight peaks evident in well-level data that are echoed in the modelled data on pore-pressure change. Note that well level serves as a proxy for pressure change, dependent on well depth and bore, inertia, storage capacity, tidal effects and atmospheric pressure: these factors are not considered in this illustrative example.



Extended Data Fig. 2 | Diffusion model results. **a.**, Pore-pressure change at 3 km below the surface (1.8 km b.s.l.) modelled over the period January 1950 to April 2019 for model Ω_1 (data shown since the 1975 Kalapana earthquake). Data modelled using gauge data are shown in red; data modelled using satellite data are in blue. Four-year averages (dashed lines) are also shown. Vertical bars indicate reported intrusion events within the rift zone. K shows the Kalapana earthquake; P represents the onset of the Pu'u 'O'o eruption; E highlights the 2018 fissure eruption. The arrow indicates the highest modelled pressure

change. **b.**, As for **a**, but for model Ω_2 , a theoretical high-diffusivity end-member scenario. **c.**, As for **a**, but for model Ω_3 , a theoretical low-diffusivity end-member scenario. **d.**, PDF of modelled pressure change at depths 1–6 km below the surface from model Ω_1 . Arrows highlight the pore-pressure front diffusing from near the surface (1 km) to greater depths over time (months and dates are shown). **e.**, As for **d**, but for model Ω_2 (pressure maxima not shown). **f.**, As for **d**, but for model Ω_3 (pressure maxima not shown).



Extended Data Fig. 3 | Predicted binomial distribution of ‘wet’ season eruptions at Kilauea. The anticipated means, \bar{x} , and standard deviations, σ , are shown. The observed number of historical ‘wet’ season eruptions (36) is

highlighted, with a probability of 0.04. Data are also shown for historical eruptions of VEI 2 and greater.

Article

Extended Data Table 1 | Parameters of models shown in Fig. 3

Layer	Property	Model			
		α	Ω_1	Ω_2	Ω_3
1	k [m ²]	1.0×10^{-12}	1.0×10^{-10}	8.3×10^{-12}	5.4×10^{-16}
	ϕ	0.3	0.2	0.2	0.2
	z [km]	0–0.5	0–0.5	0–10	0–10
	Diffusivity [m ² s ⁻¹]	3.75×10^1	5.62×10^3	4.68×10^2	3.04×10^{-2}
2	k [m ²]	6.0×10^{-15}	1.0×10^{-14}	-	-
	ϕ	0.2	0.2	-	-
	z [km]	0.5–10	0.5–1.2	-	-
	Diffusivity [m ² s ⁻¹]	3.37×10^{-3}	5.62×10^{-1}	-	-
3	k [m ²]	-	1.0×10^{-16}	-	-
	ϕ	-	0.01	-	-
	z [km]	-	1.2–10	-	-
	Diffusivity [m ² s ⁻¹]	-	1.12×10^{-1}	-	-

Models α and Ω_{1-3} are divided into up to three segments, each with a permeability, k , porosity, ϕ , and depth range, z (depth below the surface). Other parameters (K, μ) are kept constant across all models.